Modeling and Commisioning of the 10m Prototype Autoalignment System

Luis F. Ortega
Albert Einstein Institute
Max Planck Insitute
Leibniz Universität and
University of Florida Department of Physics
(Dated: August 9, 2016)

The sensitivity of a gravitational wave interferometer depends on its ability to isolate mirror motion cause by a passing gravitational wave from all other sources of mirror motion. This includes noise from our natural environment, human activity, control noise, electronic noise and the noise level of the laser light source. In the 10 meter prototype, which aims to to have a noise-floor below that of the SQL, laser frequency noise becomes a very important source of noise which needs to be dealt with. TTFSS with the frequency reference cavity subsystem at the 10m prototype aims to bring laser fluctuations to levels required for the main interefrometer experiments. Stability in the locked state of the system is paramount for the continued running of the experiments; the auto-alignment system of the reference cavity helps to bring added stability from reduced intensity noise and for the long period running of the interferometer. The focus of my time at the AEI is to measure and optimize the alignment sensing scheme used for the 10m prototype and create a proper sense-to-actuation scheme.

1. INTRODUCTION: GRAVITATIONAL WAVES AND PRECISION INTERFEROMETRY

In 1915, Albert Einstein published his work on the general theory of relativity. He aimed to explain what we perceive as gravity as being a property which arises from the curvature of space-time. Einstein proposed that large objects such as the Sun, can change the curvature of space-time, creating mountains and valleys to which smaller bodies are subject to. The gravitational force exerted by large massive objects -or any object, in an incredibly minuscule way- distorts the very fabric of space-time. Events of massive proportions, such as binary black hole mergers can create ripples in space-time as the rotating objects distort the space around them. These gravitational waves expand outwards and change the space through which they propagate depending on their polarization (fig. 1), with one direction being compressed in what we perceive to be distance and elongated in the direction orthogonal to it.

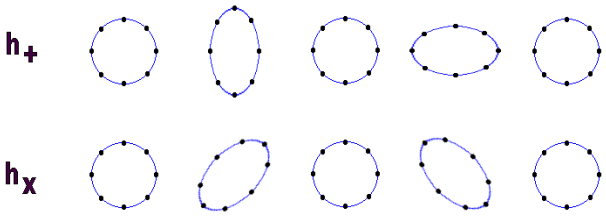

FIG. 1: Effect on test masses of Plus and X polarized gravitational waves.

We can detect these signals, which travel through the cosmos undeterred, using very sensitive optical experiments called interferometers. In gravitational wave interferometry, the experimental tool used to detect traveling gravitational waves is the Michelson interferometer. The simplest version of a Michelson interferometer consists of a coherent light source, which encounters a beam splitter and sends equal amounts of light power in orthogonal directions. There are end mirrors in each one of these directions, forming the arms of the interferometer, which reflect the light back to the beam splitter to be mixed together. The propagation of electro-magnetic fields carries an inherent phase shift, directly proportional to the propagation distance; when we mix the light fields at the beam splitter, we are gathering information of the phase shift relative to one other (eq. 1.)

$$I(x,y) = I_1 + I_2 + 2\sqrt{I_1 I_1} cos(\phi_1 - \phi_2) \tag{1}$$

Consider the effect of gravitational waves passing through the location of an interferometer; as the gravitational wave passes, the arm lengths of the interferometer change by differing amounts which changes the way in which the two signals are mixed. Using the michelson interferometer, we can sense the length change between the two arms of the interferometer by reading out the phase change between the two electromagnetic fields in the output of the interferometer. Figure 2 shows the basic setup of a michelson interferometer and the pattern formed at the output (the interference pattern after the beam splitter) with and without a signal present.

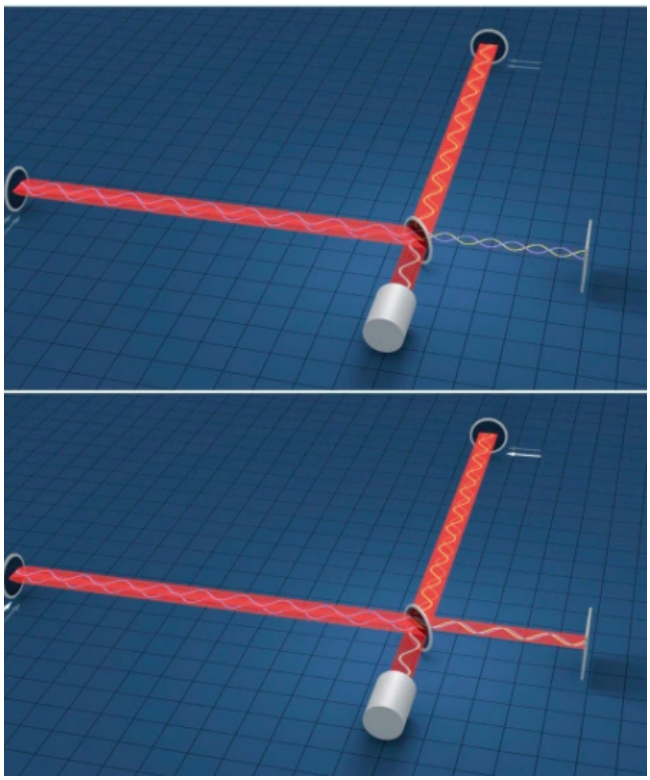

FIG. 2: Michelson interferometer, as it would be to detect gravitational waves. The interferometer is set up so that the output sits on a dark fringe (destructive interferece) When a gravitational wave passes by, the stretching and compressing of the two arms changes the way in which the waveforms are mixed and allowing light to exit the interferometer (constructive interference.)

1.1. A Momentous Day in Gravitational Wave Interferometry

In September 14 2015, LIGO (The US led effort in the study of gravitational waves, which stands for Laser Interferometer Gravitational Wave Observatory) made the first direct observation of gravitational waves using a gravitational wave interferometer (fig. 3, named GW150914). In doing so, LIGO confirmed the existence of gravitational by directly observing them for the first time in history, nearly one hundred years after Albert Einstein's work was published, and ushered in the era of gravitational wave astronomy. In December 26, a second gravitational wave event was observed (GW151226, referred to as the "boxing day event.") The continued discovery of gravitational wave events allows for an estimation of their frequency.

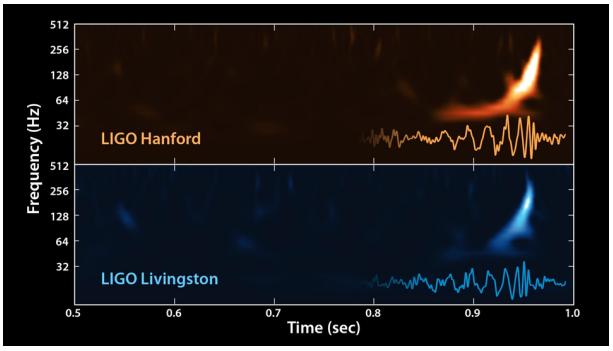

FIG. 3: LIGO measurement of gravitational wave event GW150914 at the Hanford and Livingston Observatories.

2. THE AEI 10 METER PROTOTYPE

The 10m prototype interferometer currently being built at the Albert Einstein Institute for Gravitational Physics aims to work as a test bench for future technology upgrades designed for the German gravitational wave detector GEO600. Many of the susbsystems designed by the institute have already made it to the GEO600 detector and to LIGO. The 10m prototype is not designed to be a gravitational wave detector in the sense that it is not expected that it will be able to detect gravitational wave events. The 10m prototype is designed to be a sub-SQL interferometer, reaching this remarkable sensitivity by use of the injection of squeezed states of light and the sub-systems of the prototype.

2.1. Subsystems

Vacuum System

The vacuum system for the 10m Prototype consists of 3 tanks with a diameter of 3 meters, connected by tubes of 1.5 meters in diameter. A screw pump starts the pumping of the system from atmospheric pressure. Once a pressure of 1 mbar is reached, two turbo-molecular pumps begin working, backed by a scroll pump. With this setup, the system can reach a pressure of 10^{-6} mbar within 12 hours. After a week of pumping, the system can reach a pressure of 10^{-7} mbar.

Isolation Tables

The Seismic Attenuation System is a vibration isolator which isolates the optical tables from ground noise in six degrees of freedom. The seismic attenuation is attained passively by the SAS, using the properties of mechanical isolators to attenuate above their natural frequency. The tables operate with natural frequencies of 0.05 Hz horizontally and 0.1 Hz vertically, with a target of 60 dB

attenuation at 3 Hz. The SAS is composed of the optical table which sits on 3 anti-spring filters mounted on a rigid plate, the rigid plate is supported by 3 inverted pendulum legs; a full assembly of the SAS can be seen in fig. 4. At the lowest frequencies, a collection of sensors and voice coil actuators prevent the amplification of noise at the SAS natural frequencies via electronic modal damping.

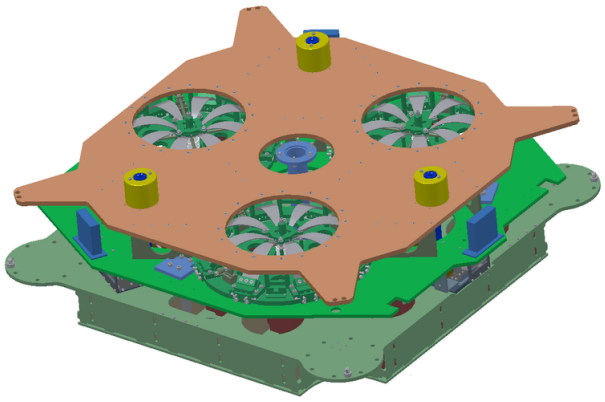

FIG. 4: Complete assembly of the Seismic Attenuation System.

Suspension Platform Interferometer

The Suspension Platform Interferometer measures the relative motion between each of the three seismically isolated tables. The relative positions are sensed and fed back to keep the tables at their initial positions by the use of actuators, aiming for a longitudal displacement of $100\text{pm}/\sqrt{Hz}$ at 10 mHz. The SPI complements the SAS as it corrects for any thermal fluctuations that may change the mechanical properties of the SAS system. This reduces the arm length fluctuations and alignment noise of the systems, also reducing the control noise of the different suspended systems.

Suspension System

The first optical system to be implemented with suspended optics is the reference cavity. The reference cavity suspension is composed of three stages of similar mass. The 850g silica optic is suspended by thin stainless wires to an intermediate aluminum mass, the intermediate mass is suspended by stainless steel wires to cantilever springs mounted on the upper stage. The upper stage is used to provide eddy current damping and for actuation on the system via magnet and coil assemblies. The upper stage is mounted on the suspension cage by a second set of cantilever blades.

Interferometer optics are suspended with a similar triple stage suspension, using masses of only 100g to reach SQL requirements. The interferometer optics will be suspended using fused silica instead, to reduce thermal noise. Other optics in the table are suspended using single stage suspensions, depending on the performance of the SAS and SPI for noise reduction.

Laser System

The 10m Prototype uses a 35W solid-state laser as the light source. The laser system begins with a 2W NPRO seed laser, which passes through four Nd:YVO4 crystals in amplifier configuration. Each crystal is pumped by a 45W (set to 33 W during normal operation) fiber-coupled laser diode. The frequency fluctuations of the 35W amplified system are the same as the 2W NPRO seed laser, which is then power and frequency stabilized to meet the required levels for the interferometer experiments.

Frequency Reference Cavity

The frequency reference cavity is a long triangular cavity, used to stabilize laser frequency to levels which meet the requirement for an SQL interferometer. The system is discussed in more detail in the next section.

3. REFERENCE CAVITY

As the 10m Prototype at the Albert Einstein Institute aims to be a sub-SQL interferometer, there are stringent frequency noise requirements to provide sufficently stabilized input light to the main interferometer.

The NPRO laser, amplified to 35W of power is very stable yet not within the requirements needed by the 10m prototype interferometer. For the frequency band of the sub-SQL interferometer, a much better frequency reference is required (about 7 orders of magnitude of noise reduction are required, shown in fig. 5.) The 10m prototype group uses two schemes to reduce freqeuncy noise; a molecular Iodine frequency reference for sub-Hertz frequencies, and a long optical resonator using suspended optics at frequencies above.

The 24.6 meter round-trip frequency reference cavity was designed to be a frequency reference in the measuremenet band of the 10m prototype intereferometer (20 Hz to ± 1 kHz.) As discussed earlier, the three mirror cavity is suspended using a triple suspension system. The cavity sits in vacuum, and locks with the aid of spot reference sensors and bosem readout sensors; the locked state is reached by using coil and magnet actuators on the top mass of the mirror suspension systems. After lock is gained, a differential wavefront sensor auto-alignment system keeps the laser input light perfectly co-aligned to the cavity mode with the use of two single suspension beam deflectors. Figure 6 shows the setup of the frequency reference system, including spot position sensors

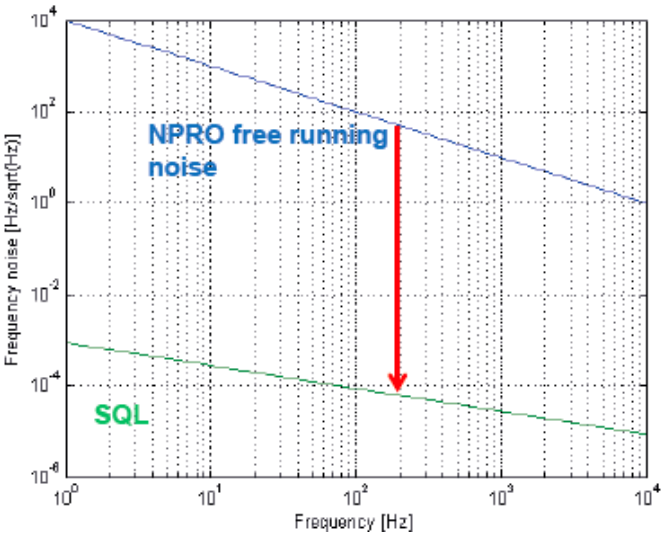

FIG. 5: Laser Frequency noise of the free-running amplified NPRO system, and the amount of noise reduction necessary for operation in the SQL interferometer.

and beam deflectors but not the differential wavefront system which is discussed later on.

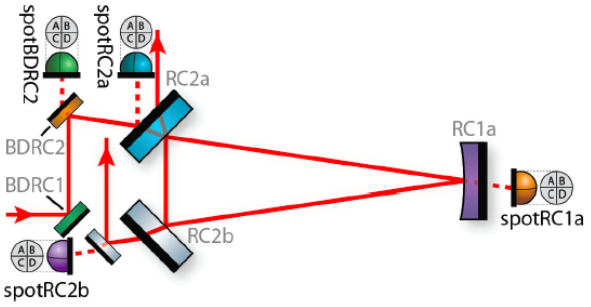

FIG. 6: Frequency reference cavity setup; the spot position sensors are colored to the optics for which they serve as a reference to in the initial alignment of the system.

4. DIFFERENTIAL WAVEFRONT SENSING

Differential wavefront sensing is a powerful auto-alignment technique which controls the angular degrees of freedom of a triangular optical resonator. The system aims to stabilize the light entering the main interferometer, suppressing noise and adding stability to the locked-state of the system. In our experimental setup, the alignment signals created by the DWS technique are fed back to two beam deflectors (suspended steering mirrors which can be remotely controlled to co-align the incoming beam to the cavity eigenmode.) A summary of the details on which a differential wavefront system auto-alignment scheme are based on follows.

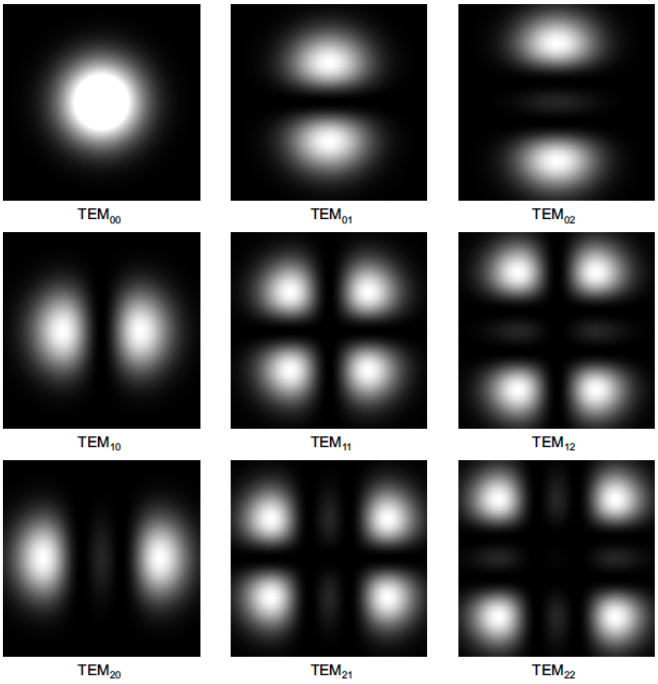

FIG. 7: Intensity profiles of Hermite-Gaussian modes (TEM modes). These are approximate solutions of the wave equation.

Laser light in the vacuum system is phase-modulated with an 8 MHz sine waveform; the resonance condition of the optical resonator in perfect alignment requires that all carrier light is transmitted, but the two sidebands created by phase modulatation are not. They are completely reflected from the cavity, being ±8 MHz away from the carrier frequency. If the cavity is not perfectly aligned (the input beam does not perfectly coincide with the cavity mode,) then some of the carrier light is reflected from the cavity in the form of TEM higher-order modes (fig. 7.) The reflected light field in TEM_{01}/TEM_{10} modes beats with the TEM_{00} sidebands to create an intensity distribution with symmetry around the x/y axis. Taking advantage of this symmetrical distribution, we can find the difference in total intensity between each side (between top and bottom of y = 0 for TEM_{01} and between left and right of x = 0 for TEM_{10} misalignments.) This yields an error signal which is proportional to the amplitude of the misalignment mode, and which carries information of the relative phase of the misalignment mode.

$$Err(t) = \sqrt{8\pi}a\cos[\theta]\sin[\Omega t]$$

Information of the relative phase of the misalignment mode allows a distinction between tilt and translation misalignment: If the mirror is offset, $\theta = 0$; thus a photodiode very close to the cavity (avoiding phase change due to propagation, to maintain $\theta = 0$) will be very sensitive to misalignment due to offset with respect to the cavity waist (near-field). If the mirror is tilted, then $\theta = \frac{\pi}{2}$ and we are not sensitive to tilt misalignment at this first photodiode position. If we allow the beam to propagate, then θ will oscillate to $\theta = 0$ again; a photodiode at this point would be very sensitive to tilt misalignment (far-field). The error signal oscillates at the modulation frequency (Ω) of 8 MHz. I-phase demodulation (times $\sin(\Omega)$, averaged over one cycle) produces a constant signal proportional to the misalignment.

5. DETECTION BENCH OPTICAL SETUP

Reflected light from the Reference Cavity is let out via viewports at the central table, and is directed to the Detection Bench out of vacuum. The beam is lowered via a periscope and some of the power is dumped using a half-wave plate polarizer and a polarizing beam splitter; the light fields within the detection bench should be p-polarized for this reason. The beam is focused through a series of lenses to properly control the gouy phase propagation into the wavefront sensors. This lensing system includes a gouy phase telescope which attemps to create a gouy phase accumulation of as close to 90 degrees as possible between wavefront sensor 1 and 2 (WFS1 and WFS2.) A visual representation of the optical setup of the detection bench can be seen in figure 8.

The light incident onto each wavefront sensor is first incident on a galvo motor to control the beam centering system onto each wavefront sensor. This is composed of a simple DC readout scheme as shown in table I.

TABLE I: WFS DC readout scheme for beam centering. The DC power on each quadrant of the WFS are recombined as specified in the table, and fed back to the galvo motors to keep the beam equally on all four.

	Quadrant A	Quadrant B	Quadrant C	Quadrant D
Pitch	1	1	-1	-1
Yaw	1	-1	-1	1

The beam incident onto wavefron sensor 2 is also imaged through a series of lenses and mirrors into the Pound-Drever Hall locking diode. This setup takes advatage of the centering system in place for the wavefront sensor to also keep light incident in the photodiode responsible for keeping the laser frequency tuned to the cavity eigenmode for the fundamental mode of light. Before reaching the locking photodiode, a large amount of the power is dumped to protect the photodiode and to maintain a stable servo loop.

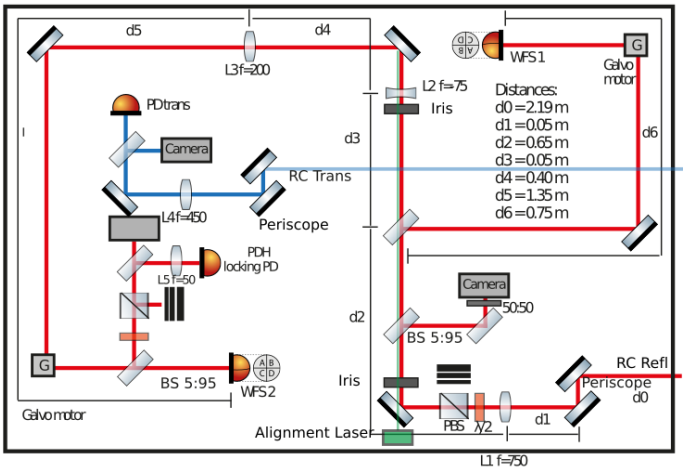

FIG. 8: Optical setup of the detection bench for the Reference Cavity. Focal lengths are specified in mm. The WFSs have 3 mW of power incident on them when the cavity is unlocked.

5.1. Wavefront Sensors

The wavefront sensor used for the autoalignment system of the reference cavity are similar in construction and quality to wavefront sensors used by GEO600. They are composed of DC biased quadrant photodiodes, capable of handleing incident power of around 15mW. The photodiodes feed to DC and RF readout schemes, with an RF resonant circuit at 8 MHz (fig. 9), which is the modulation frequency for both PDH sensing and the differential wavefront sensing autoalingment scheme.

The wavefront sensors feed the output data to CDS, which is then viewed or utilized via computer systems. Within CDS, there are some corrections made to the signals output by the wavefront sensors. The RF readout has to be rotated, for two reasons: once the beam exits the vacuum system, it is higher in height than the detection bench optics, thus a periscope is introduced at the input of the detection bench setup; this rotates the beam by 90 degrees. The galvo motors prior to the each wavefront sensor also introduce a slight rotation of the beam. Further, the DC readout scheme is normalized to the total amount of incident light onto the wavefront sensors.

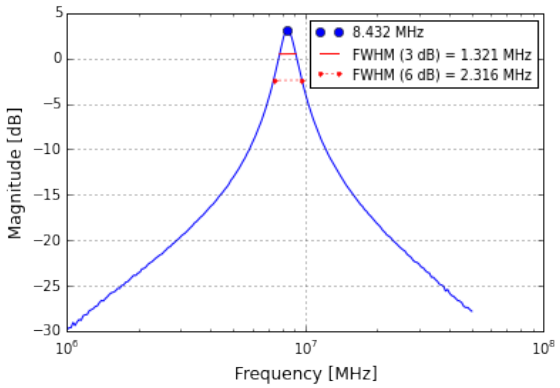

FIG. 9: Transfer function using a network analyzer. The NA output excites a test laser and is also fed to input A, the RF sum output of the WFS is fed to input B. The B/A measurement is displayed. Calculated from the data is the resonance at the curve peak and FWHM at 3 and 6 dB.

5.2. TTFSS

Within the detection bench is the locking photodiode responsible for Pound-Drever Hall frequency stabilization. The Pound-Drever Hall error signal is created from the same 8MHz modulation applied for the autoalignment system and is used by the Table Top Frequency Stabilization Servo (TTFSS, a system borrowed from aLIGO) to reduce frequency noise. The system utilizes three different actuators for different frequency ranges: laser temperature control (less than 1 Hz,) piezo control (1 Hz to 10 kHz) and an EOM (more than 10 kHz.) The noise suppression requirements for the prototype, and and the noise suppression performance of the TTFSS are displayed in figure 10.

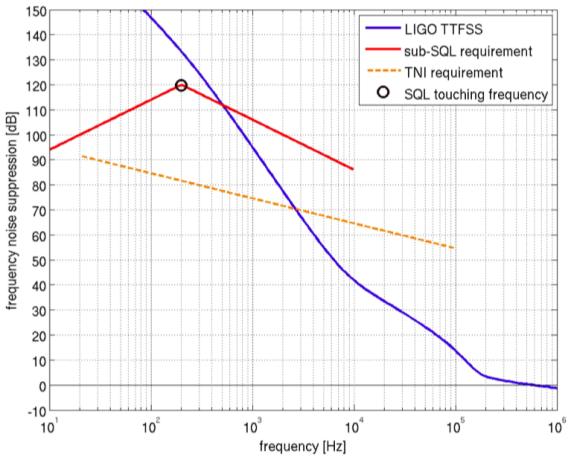

FIG. 10: Frequency noise suppression requirements for the AEI 10m Prototype and performance of the TTFSS.

6. MODELING THE AUTOALIGNMENT SYSTEM

While getting the differential wavefront sensing system to optimal operation using the set sensing and driving matrices already present at the beginning of the experiment, I also ran a Finesse simulation of the optical setup. The kat file used for the simulation begins from a lens before the reference cavity, through the two beam deflectors and includes the detection bench and both wavefront sensors. The details and results of the simulation will be presented in this section, in a progression which generally follows the steps that were taken in ensuring the correct setup and working of the system.

The first step in ensuring the proper setup of the differential wavefront sensing system was to check that progation distances and lenses allow for the correct Gouy phase separation between WFS1 and WFS2. The lenses for the system had already been picked and setup by the AEI team, so it only made sense to check in simulation that the distances in the setup were correctly setup. The distance between reference cavity beam deflectors (these will be referred to as BDRC1 and BDRC2 going forward,) is sweeped and gouy phase difference measured (eq. 6) using finesse. Result of this sweep measurement can be seen in fig. 11, we were aiming for a gouy phase difference around of around 90 degrees between them. More importantly, the gouy phase difference between WFS1 and WFS2 is measured next by sweeping the distance between lens L2 and WFS2. Result of this sweep can be seen in fig. 12.

$$\psi(z) = arctan(\frac{z}{z_0}) \tag{2}$$

The gouy phase propagation was calculated with all components of the system included, with the distances used to set up the physical optical system in the kat file. This computation uses finesse to calculate gouy phase differences between set minuscule points of the system, so that it sweeps distance in very small steps and outputs the gouy phase difference between them. These are added all together to create a plot of the gouy phase through the different components, which can be seen in fig. 13.

After properly setting up the components which allow for detection of the tilting wavefronts in both quadratures (separated by the 90 degree gouy phase,) the proper demodulation phase for each wavefront sensor is set. In simulation, the demodulation phase of WFS1 and WFS2 is swept through 360 degrees while taking a numerical derivative with respect to motion applied to the end mirror of the triangular cavity ('diff' command in finesse.)

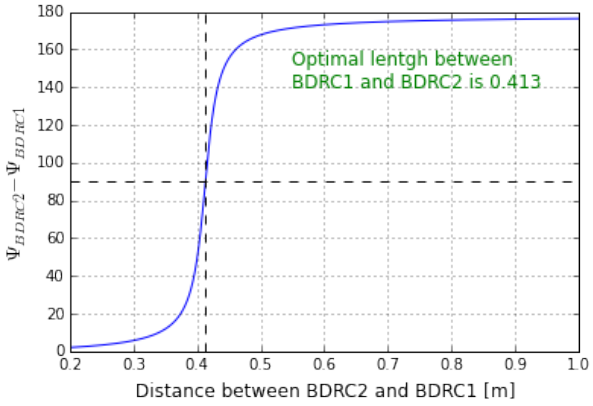

FIG. 11: Accumulated gouy phase between BDRC1 and BDRC2, as the distance between the two is increased from 0 to 2 meters. A vertical and horizontal lines mark the point at which the gouy phase separation is 90 degrees.

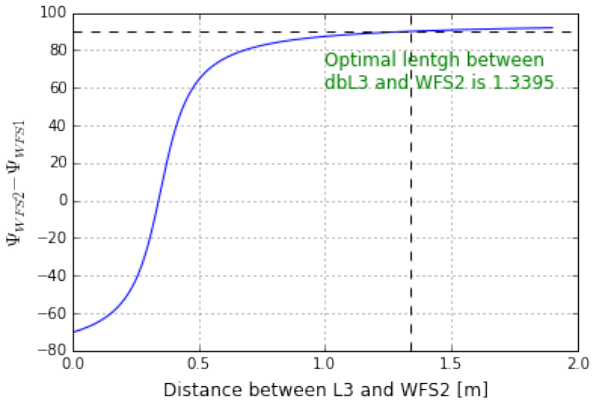

FIG. 12: Accumulated gouy phase between WFS1 and WFS2, as the distance between the two is increased from 0 to 2 meters. A vertical and horizontal lines mark the point at which the gouy phase separation is 90 degrees.

The output is a set of slopes of the error signal generated by the Pound Drever-Hall frequency stabilization scheme, the optimal demodulation phase is the point at which this slope is highest. A plot of these slopes is shown in fig. 14.

Experimentally, the process by which the demodulation phase is chosen is less precise. The demodulation phase is set by way of a phase shifter which is controlled by the amount of voltage applied. The device is nonlinear, and it is not well-characterized; the amount of voltage applied to it is visible in CDS, but there is no conversion to degrees. The reference cavity mirrors are suspended optics, so length actuation (as in the simulation) is harder to properly drive, the NPRO laser's temperature channel was instead excited at 10Hz. The signal

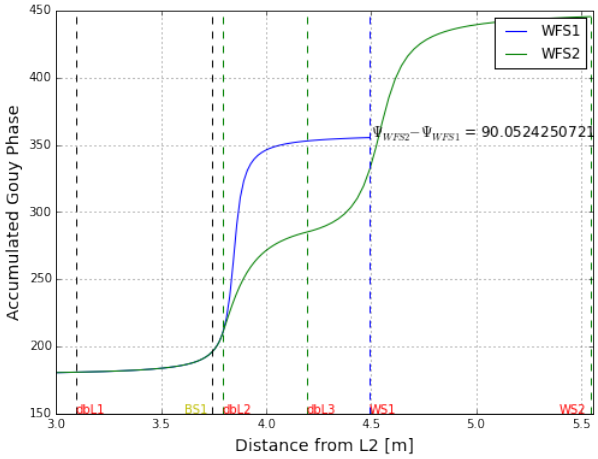

FIG. 13: Calculated accumulated gouy phase in the Reference cavity system. Lens L2 is the lens prior to beam deflectors 1 and 2. Vertical markings correspond to the physical placement of the annotated components, with the color corresponding to the path of either WFS1 or WFS2.

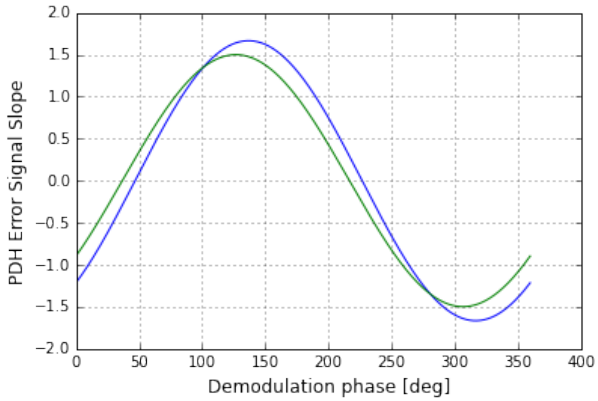

FIG. 14: WFS1 and WFS2 signal slope through varying demodulation phases. Optimal demodulation phase is set at the peak of the curve, where the error signal slope is largest.

seen on individual segments of the two WFSs was measured via the system's diagnostic test tool (DTT) via a sine response measurement with continuous averaging (so that as the demodulation phase is changed, the output of the measurement displays the increase or decrease in the separation of signals.) The demodulation phase is changed through the range of the phase shifter (approximately 180 degrees,) and set to the voltage at which the signal at each wavefront sensor is the largest.

In simulation, once the right gouy phase separation and demodulation phase are set, we are ready to generate alignment signals. Beam deflector drives are actuated one by one (BDRC1 in pitch,yaw and BDRC2 in

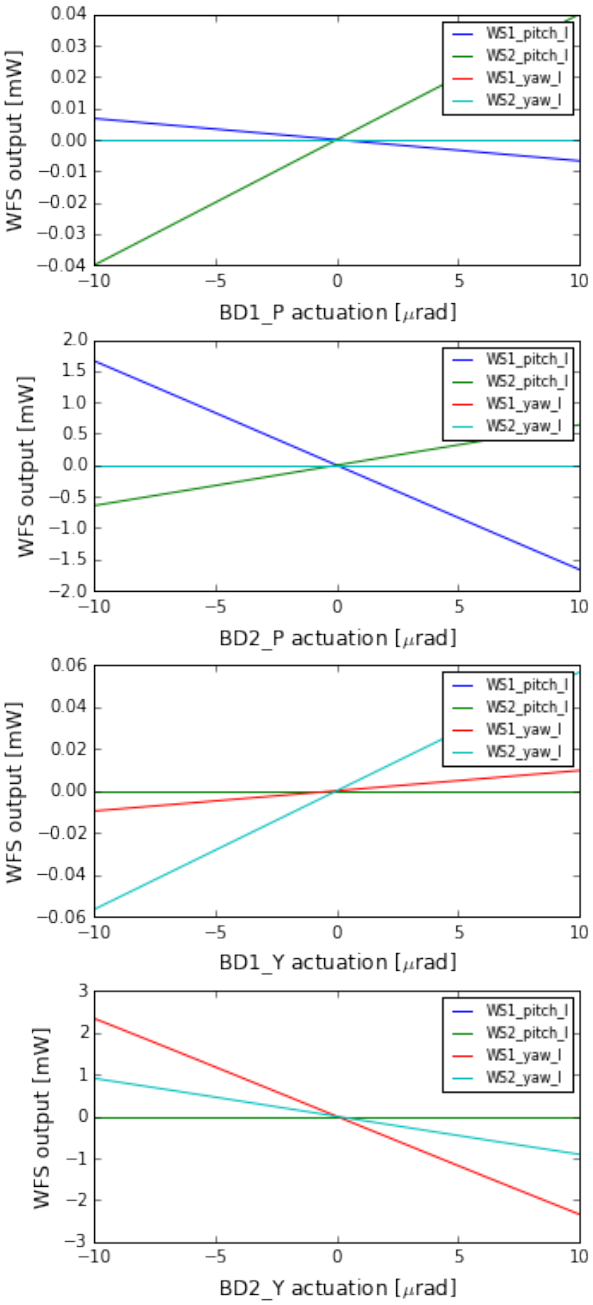

FIG. 15: Simulated signals using Finesse; WFS signals created by beam deflector drive.

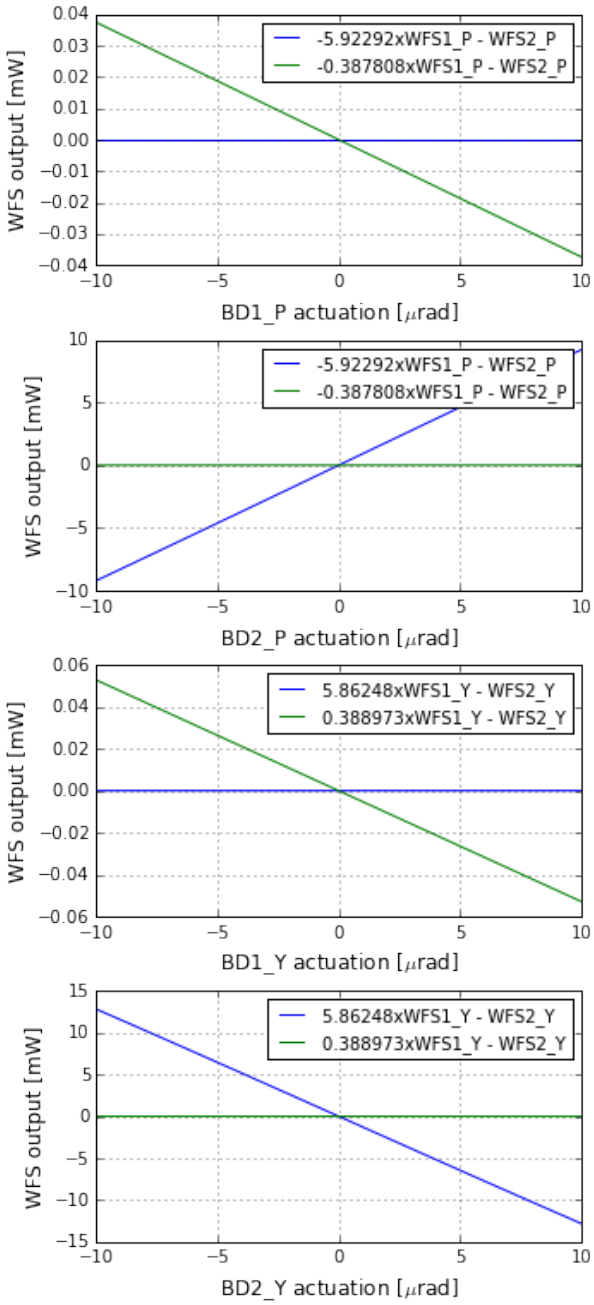

FIG. 16: Simulated signals using the sensing DOFs as described in eq. 3.

pitch,yaw.) The simulation is run for each beam deflector drive, which outputs all expected signals from WFS1 and WFS2. The alignment signals are plotted in figure 15. Each plot contains the alignment signals expected per amount of beam deflector actuation. The alignment sensing matrix is output and displayed in table II.

From figure 15, we observe the current sensing matrix produces a mix of signals from both WFS1 and WFS2 for each of the individual drives we have declared. As it is expected, a drive in pitch creates no yaw misalignment and a drive in yaw creates no pitch misalignment. We have originally labeled our degrees of freedom assuming that motion from BDRC2 would only be measured by WFS1, and motion from BDRC1 would only be mea-

sured by WFS2. We can now re-state our sensing degrees of freedom by recombining wavefront sensor signals in such a way that we create a sensing matrix for which each beam deflector drive is only sensed by each new declared degree of freedom. This results in a clear speration in sensing between BDRC1 actuation and BDRC2 actuation, as seen in figure 16. The new sensing degrees of freedom are stated in eq. 3, where the factors being multiplied by are the ratios $\frac{WFS2}{WFS1}$ sensed with each BDRC drive (table II.)

TABLE II: Simulated alignment sensing matrix using Finesse, each entry being the slope of the expected error signal to be created by beam deflector displacement.

	$WFS1_{pitch}$	$WFS2_{pitch}$	$WFS1_{yaw}$	$WFS2_{yaw}$
$BDRC1_{pitch}$	-675.035	3998.18	0	0
$BDRC2_{pitch}$	-166833	64699.4	0	0
$BDRC1_{yaw}$	0	0	966.954	5668.75
$BDRC2_{yaw}$	0	0	-235972	-91787

$$\begin{aligned} BDRC1_{pitch} &= -0.38781 \times WFS1_{pitch} - WFS2_{pitch} \\ BDRC2_{pitch} &= -5.9229 \times WFS1_{pitch} - WFS2_{pitch} \\ BDRC1_{yaw} &= 0.38897 \times WFS1_{yaw} - WFS2_{yaw} \\ BDRC2_{yaw} &= 5.8625 \times WFS1_{yaw} - WFS2_{yaw} \end{aligned} \tag{3}$$

7. RESULTS

Once gouy phase difference in our optical system has been modeled and ensured to be close to 90 degrees in separation between WFS1 and WFS2, I began tweaking the specifics of the system to ensure optimal performance. Besides the correct demodulation phase, the procedure for which was already described, the wavefront sensors also need to be applied a sector rotation to account for both the periscope at the input of the detection bench and the galvo motors prior to each wavefront sensor. A sine response measurement with exponential averaging is performed, and the rotation in degree is changed until finding a peak in the separation between pitch and yaw signals at each wavefront sensor. The measurement is performed for each WFS degree of freedom (pitch or yaw) and is reapeated to ensure the right rotation angle. Both WFS sensors are set to have a rotation of 86 degrees performed on the RF output.

To ensure the reading of alignment signals is not limited by noise, both a dark measurement of the WFS RF output is measured, as well as a measurement with light on and with all beam deflector channels driving mirror motion at separate frequencies. The results of both measurements show that cavity mode misalignments are visible above the WFS noise floor. Figure 17 shows the frequency spectral density measurement of the WFS when there is no light incident on the QPD; both WFSs show the noise floor to be at same level. Figure 18 displays a sine response measurement for both wavefront sensors. All beam deflector drives (BDRC1 pitch and yaw, BDRC2 pitch and yaw) are actuated for this single measurement, each at a different frequency. The result shows the WFS response to misalignment is clearly visible above the noise floor. The noise floor seen in WFS2 with light incident is one order of magnitude higher than that of WFS1, a higher sensitivity to random cavity mirror motion could explain the difference.

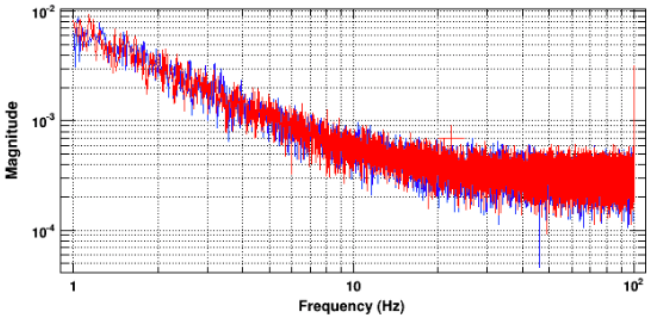

FIG. 17: Measured noise floor for WFSs when no light is incident on the photodiode.

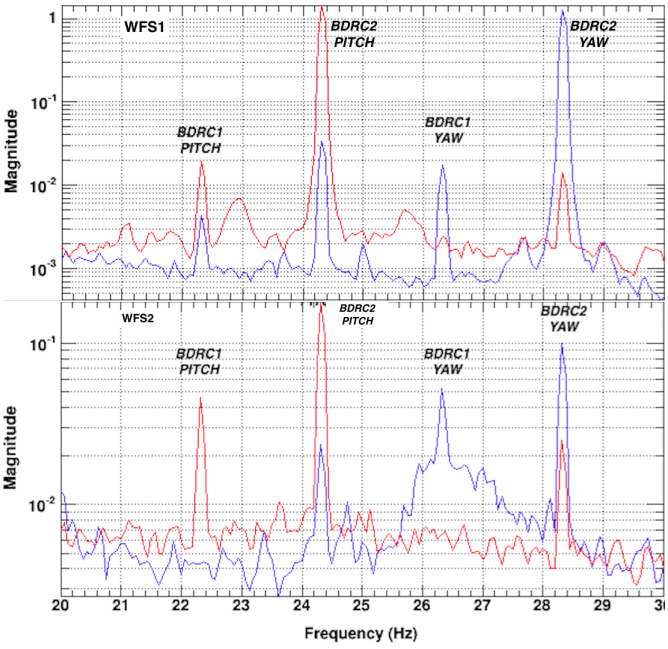

FIG. 18: Measured magnitude of misalignment signal on each WFS. All BDRC drives are actuated at different frequencies.

Once a clear visibility of misalignment signals and the setup of the differential wavefront sensing optical system is ensured, we can begin to take transfer functions to view the behavior of the system across the frequency range we expect the system to function in. Each beam deflector drive is actuated separately and a long measurement is performed. From our simulation results, we expect that each beam deflector drive will create error signals in both WFS1 and WFS2; our sensing matrix assigns BDRC1 actuation to a sense degree of freedom of only WFS2, and BDRC2 actuation to a sense degree of freedom of only WFS1. The output of our measurement can be used to create a new sensing matrix with which each new sensing degree of freedom will only be sensitive to a specific beam deflector drive.

Because the resulting matrix is not mathematically diagonalizable, a different approach in creating a sensing matrix which will isolate beam deflector drives is used. I will use the following numbers for an example:

$$BDRC1_{pitch} = WFS1_{pitch} + 2 \times WFS2_{pitch}$$
$$BD2RC_{pitch} = 2 \times WFS1_{pitch} + WFS2_{pitch}$$

We can create a combination of WFS1 and WFS2 which is insensitive to $BDRC1_{pitch}$, as well as one that is insensitive to $BDRC2_{pitch}$. Taking advantage that the new DOF which is insensitive to $BDRC1_{pitch}$ will not be insensitive to $BDRC2_{pitch}$, the new sensing matrix would be:

$$DOF1_{pitch} = 2 \times WFS1_{pitch} - WFS2_{pitch}$$
$$DOF2pitch = 2 \times WFS2_{pitch} - WFS1_{pitch}$$

$DOF1_{pitch}$ will only be sensitive to $BDRC2_{pitch}$ and $DOF2_{pitch}$ will only be sensitive to $BDRC1_{pitch}$. The same approach is taken to create yaw misalignment sensing channels.

The transfer function measurements yield the results shown in figures 20 for pitch actuation of each beam deflector, and 21 for yaw actuation of each beam deflector. The magnitude of the transfer coefficients for each beam deflector drive are summarized in table III; these values are used as described in the above approach to create a sensing matrix with which beam deflector drives are separated. These new sensing degrees of freedom are displayed in equation 4.

$$\begin{aligned} BDRC1_{pitch} &= 0.1667 \times WFS1_{pitch} - WFS2_{pitch} \\ BDRC2_{pitch} &= 2.1178 \times WFS1_{pitch} - WFS2_{pitch} \\ BDRC1_{yaw} &= 0.007282 \times WFS1_{yaw} - WFS2_{yaw} \\ BDRC2_{yaw} &= 3.5023 \times WFS1_{yaw} - WFS2_{yaw} \end{aligned} \quad (4)$$

TABLE III: Measured transfer coefficients for wavefront sensor misalignment signal for by beam deflector drive at 0.1 Hz.

	$WFS1_{pitch}$	$WFS2_{pitch}$	$WFS1_{yaw}$	$WFS2_{yaw}$
$BDRC1_{pitch}$	2.377×10^7	5.034×10^7	0	0
$BDRC2_{pitch}$	1.77×10^9	2.95×10^8	0	0
$BDRC1_{yaw}$	0	0	4.814×10^6	1.686×10^7
$BDRC2_{yaw}$	0	0	4.93×10^8	3.59×10^6

The approach used in creating a diagonalized sensing matrix assumes that when BDRC1 and BDRC2 actuation is applied in the system, no yaw misalignment is sensed at the wavefront sensors. While this would be true in an ideal system, some yaw misalignment is sensed when applying pitch misalignment in our system and vice-versa. While these signals are small enough to be considered negligible for our purposes, it will be advantageous to reduce their presence further or eliminate entirely. Measurements using the spot position QPDs present for cavity alignment suggest that the source of this coupling is due to differences in strength of the coil drivers in each of the corners of the beam deflectors; figure 19 shows the beam deflector assembly and the current driving matrix used for each beam deflector drive.

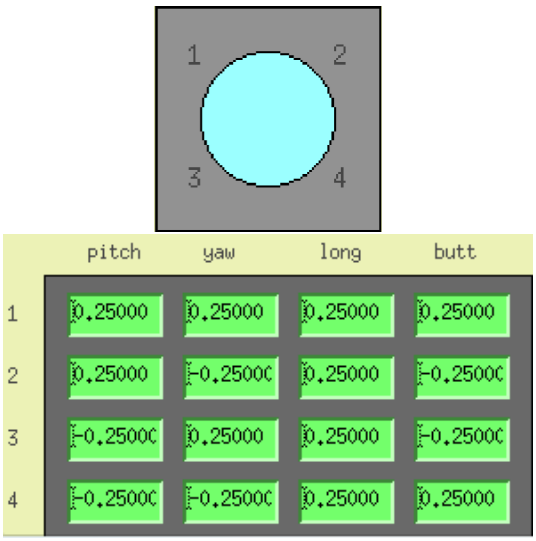

FIG. 19: Driving matrix for the beam deflectors, with an illustration of the way in which the matrix is applied physically.

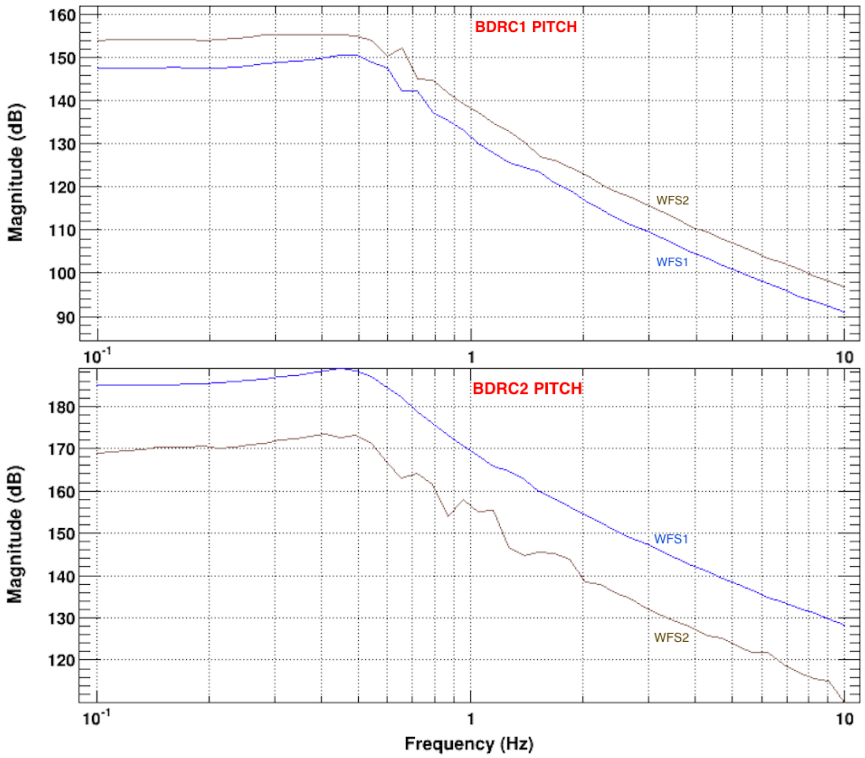

FIG. 20: Measured transfer function for wavefront sensor misalignment signal by beam deflector pitch drive.

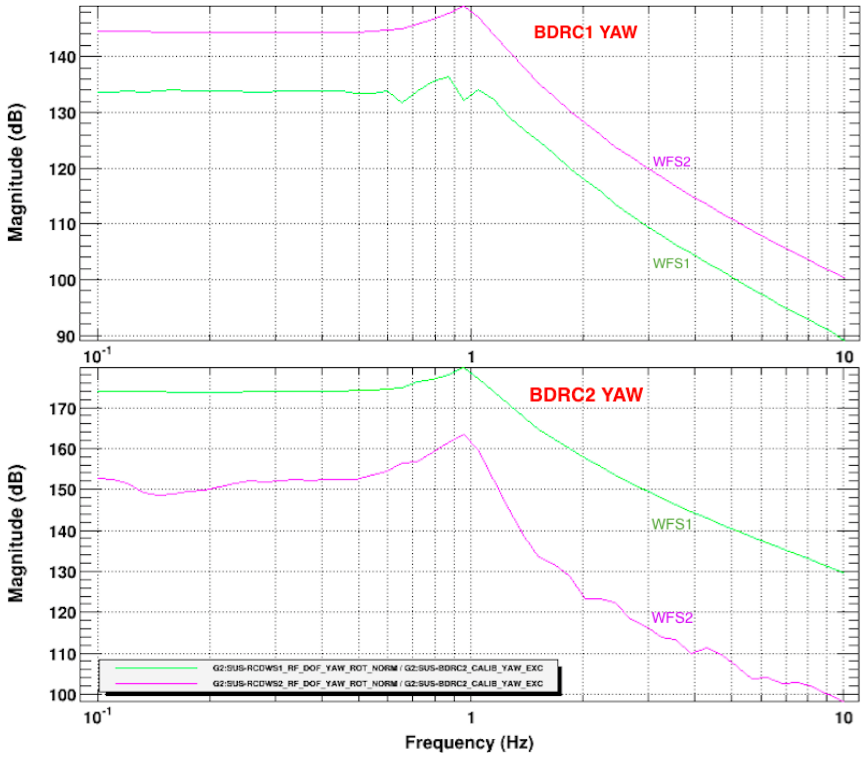

FIG. 21: Measured transfer function for wavefront sensor misalignment signal by beam deflector yaw drive.

8. FURTHER WORK

As discussed in the results section of the paper, an error with the beam deflector magnet and coil driving system is apparent. For further optimization of the system, a characterization of the system to adjust the gains for the coils at each of the corners of the beam deflectors is the next step to be taken in optimizing the differential wavefront sensing system. Driving each corner with the same amplitude and looking at the signal response on the spot position sensors (normalized to the amount of light incident to account for inhomogeneities on the detector surface) would be an appropriate way to attempt at a characterization of the coil and magnet actuators in each of the corners.

Acknowledgements

I would like to give special acknowledgement to the members of the group at the AEI 10m Prototype, all of whom showed a great deal of consideration to me and my efforts in this project. My gratitude goes out to Haral Lück, David Wu, Manuela Hanke, Tobias Westfall (Fu), Gerald Bergmann, Sina Kölenbeck, Vaishali Adya, Patrick Oppermann and Janis Woehler for making my stay at the AEI fun and succesful and providing help and instruction for the duration of my project. I'd also like to thank the University of Florida, Guido Müller, Bernard Whiting, Michaela Pickenpack, Kristin Nichola, Ryan Goetz, all staff involved in the planning this summer IREU, and the NSF for providing the funding for this research opportunity.

[1] A. E. Institute, *AEI 10m Prototype* (2016), URL http://10m-prototype.aei.uni-hannover.de/.

[2] M. Eichenfield, *Modelling and Commissioning the Wavefront Sensing Auto-Alignment System of a Triangular Mode Cleaner Cavity* (LIGO-T030234-00-DA, 2003).

[3] R. Naeye, *Gravitational Wave Detection Heralds New Era* (2016), URL http://www.skyandtelescope.com/astronomy-news/gravitational-wave-detection-heralds-new-era-of-science-021

[4] T. Pile, *Most Precise Ruler Ever Constructed* (2016), URL https://www.ligo.caltech.edu/video/ligo20160211v6.

[5] M. Hanke, *Laser frequency stabilization for the aei 10m prototype* (2013).